Modeling the Inhibition Effect of Straw Checkerboard Barriers on Wind-blown Sand

Haojie Huang[1,2,3]

[1]School of Energy and Power Engineering, University of Shanghai for Science and Technology, Shanghai, PR China

[2]MOE Engineering Research Center of Desertification and Blown-sand Control, Beijing Normal University, Beijing, PR China

[3]College of Mechanics and Materials, Hohai University, Nanjing, Jiangsu 211000, PR China

Correspondence: H.J. Huang (hjhuang@usst.edu.cn)

Abstract

Straw checkerboard barriers (SCBs) are usually laid to prevent or delay desertification caused by aeolian sand erosion in arid and semiarid regions. Understanding the impact of SCBs and their laying length on aeolian sand erosion is of great significance to reduce damage and laying costs. In this study, a three-dimensional wind-blown sand model in the presence of SCBs was established by introducing the splash process and equivalent sand barriers into a large-eddy simulation airflow. From this model, the inhibition effect of SCBs on wind-blown sand was studied qualitatively, and the sensitivity of aeolian sand erosion to the laying length was investigated. The results showed that the decrease in the wind speed in the SCB area oscillates along the flow

direction. Moreover, the longer the laying lengths are, the lower the wind speed and the sand transport rate in the stable stage behind SCBs will be. We further found that the concentration of sand particles near the side of SCBs is higher than that in its central region, which is qualitatively consistent with previous research. Our results also indicated that whether the wind speed will decrease below the impact threshold or the fluid threshold is the key factor affecting whether sand particles can penetrate the SCBs and form stable wind-blown sand behind the SCBs under the same conditions. Although our model does not include the collision between sand particles and SCB walls, which makes the suppression of wind-blown sand by SCBs obtained from the current model conservative, our research still provides theoretical support for the minimum laying length of SCBs in anti-desertification projects.

1. Introduction

In arid and semiarid areas, aeolian sand erosion is becoming increasingly serious. Preventing or delaying the process of desertification is a major challenge worldwide, especially in the transitional areas between deserts and oases. At present, shelterbelts (Wang et al., 2010), sand fences (Bitog et al., 2009; Hatanaka and Hotta, 1997; Li and Sherman (2015); Lima et al., 2017; Pye and Tsoar, 2008; Wilson, 2004), wind-break walls (Bouvet et al., 2006; Santiago et al., 2007), hole plate-type sand barriers (Chen et al., 2019) and straw checkerboard sand barriers (Bo et al., 2015; Huang et al., 2013; Wang and Zheng, 2002; Xu et al., 2018) are the main structures used to prevent desertification. Among these structures, straw checkerboard barriers (SCBs) are the most commonly used in anti-desertification projects because of their advantages of

45 being easy to obtain and relatively low cost (Zheng, 2009). Laying SCBs could play

46 an important role in the ecological restoration of sandy land ecosystems (Zhang et al.,

47 2018) and vegetation restoration. Some research has shown that SCBs can effectively

48 reduce the surface wind speed (Qu et al., 2007), increase the surface roughness

49 (Zhang et al., 2016), weaken the sand transport rate (Bo et al., 2015), and change the

50 distribution of aeolian sandy soil particles and soil organic carbon (Dai et al., 2019),

51 thus protecting the survival of vegetation and achieving sustainable development of

52 oases and ecological environments.

53   In recent decades, SCBs have been widely used in Northwest China, which is

54 seriously damaged by aeolian sand erosion. For example, SCBs have been laid on the

55 sides of roadbeds along railways such as the Baotou-Lanzhou Railway, Wuda-Jilantai

56 Railway (Wang, 1996), Gantang-Wuwei Railway (Yang, 1995), Lanzhou-Xinjiang

57 Railway (Binwen et al., 1998; Cheng et al., 2016), and Qinghai-Tibet Railway (Cheng

58 and Xue, 2014; Zhang et al., 2010), as well as in windy sand areas beside desert roads

59 such as the Taklamakan Desert Highway (Li et al., 2006; Qu et al., 2007), Tarim

60 Desert Highway (Xu et al., 1998) and Minqin Desert Highway. In addition, SCBs are

61 adopted by some countries that are also affected by aeolian sand erosion, such as

62 Ghana, Egypt, and Iran (Zheng, 2009). Although SCBs have been widely used, their

63 design size and laying methods are mainly determined by practical experience or

64 repeated tests. For example, for the sand fence, which has a similar effect to the SCB,

65 Li and Sherman (2015) combined experimental and field data to conclude that the

66 optimal design of a sand fence is closely related to its aerodynamics and

67 morphodynamics. The effect of sand fences with different porosities, spacings and

68 heights on the wind field is significant (Lima et al., 2017; Lima et al., 2020). However,

69 the complexity of the flow field around the SCBs and the movement of sand particles,

70 as well as the coupling of particles and flow field, make this problem more difficult.

71 Therefore, it is necessary to study the characteristics of turbulence inside and behind

72 the SCBs as well as the influence mechanism of the laying length on wind speed and

73 erosion.

74   Wang and Zheng (2002) proposed an ideal single-row uniformly distributed

75 vortex model to simplify the flow field of wind-blown sand. Based on their model, the

76 corresponding relationship between the side length and the height of a single SCB

77 was analysed. Their theoretical results are similar to the size of the SCBs laid in the

78 Tarim Desert Highway (1 m in side length and 15-20 cm in height). Qiu et al. (2004)

79 noted that since the concentration of wind-blown sand below 10 cm near the surface is

80 relatively high, the height of the SCBs should be designed to be 10-20 cm to

81 effectively prevent aeolian sand erosion. The experimental results of Zhang et al.

82 (2018) indicated that the SCB has the best protective effect when its side length is 1 m.

83 These works are of great help to the design of a single SCB. Based on these empirical

84 sizes of the SCBs, researchers have tried to analyse the effect of SCBs on the flow

85 field and particles from the perspective of turbulence. Huang et al. (2013) used a

86 two-dimensional large eddy simulation and discrete particle tracking methods to

87 simulate wind-blown sand movement inside simplified two-dimensional SCBs. The

88 effect of SCBs on surface wind speed was analysed. They found that sand particles

89 could be aggregated at the inner walls of the SCBs due to the influence of the vortex

90 or the backflow. Then, a V-shaped sand trough was formed, which is similar to the

91 actual situation. Bo et al. (2015) equated the SCBs to the source term of the standard

92 $k\text{-}\varepsilon$ turbulence model and analysed the influence of SCBs on the wind speed profile in

93 a two-dimensional flow field without sand particles. They divided the streamwise

94 velocity profile in a flow field containing SCBs into approximately three different

95 log-linear functions and obtained the relationship between them and friction wind

96 speeds. Although these two-dimensional models can reflect the effect of the SCBs on

97 the flow field to some extent, they are far from the real turbulence. Moreover, since

98 the three-dimensional SCB is simplified into a two-dimensional plane with only the

99 streamwise direction and vertical direction, the impact of this simplification is

100 uncertain. For this reason, Xu et al. (2018) simulated wind-blown sand movement on

101 the SCB surface under a three-dimensional flow field using OpenFOAM and mainly

102 analysed the influence of the flow field inside the SCBs on the movement of sand

103 particles. They concluded that the wind vortex is the main cause of the internal

104 morphology of the straw checkerboard. They found that the vortex drives particles

105 inside the SCBs towards the front and sidewalls, making the erosional form in SCB

106 cells low in the middle and high near all sides. However, the SCBs are completely

107 equivalent to the solid as the bottom boundary condition in their model. As a nonsolid

108 material, SCBs can be penetrated by wind in practice. It only weakens the wind speed

109 and is thus not equivalent to a solid. For example, Dupont et al. (2014) equated

110 surface vegetation to a resistance force through the resistance coefficient and leaf area

111   coefficient, that is, the wind will be resisted as it passes through these equivalent

112   regions.

113   To reasonably introduce the SCBs and consider their coupling with turbulence,

114   SCBs and the surface splash process, the development of a three-dimensional model

115   is needed. In this paper, a three-dimensional numerical coupled model of wind-blown

116   sand in the presence of SCBs was carried out to study the inhibition effect of the

117   laying length on aeolian sand erosion. The large eddy simulation approach was used

118   to simulate clean air flow with the saltation process. Furthermore, we added a volume

119   drag force into the Navier-Stokes equations by using the drag source method to realize

120   the coupling between the SCBs and the wind-blown sand movement. Section 2 and

121   Section 3 present the three-dimensional numerical coupled model and its validation,

122   respectively. In Section 4, the effects of the SCB laying length on clean air flow and

123   sand-laden flow under different friction wind speeds are studied. Finally, Section 5

124   summarizes the main conclusions.

125   **2. Models**

126   The Advanced Regional Prediction System (ARPS) has been widely used to

127   simulate turbulent boundary-layer particle-laden flow, such as wind-blown sand

128   (Dupont et al., 2013; Huang, 2020) and wind-blown snow (Huang and Wang, 2016; Li

129   et al., 2018). The standard version of the program is described in the ARPS User's

130   Manual (Xue et al., 1995), and its validation cases are referred to Xue et al. (2000)

131   and Xue et al. (2001). For this study, some suitable models were added to simulate

132 turbulent boundary-layer flow in the presence of SCBs with saltating sand particles. A

133 detailed description of these modifications is shown in the following subsections.

134 **2.1 Turbulent boundary-layer flow**

135 The basic flow fields in our numerical simulation are established based on ARPS

136 (version 5.3.4). The filtered continuity and momentum equations, including the

137 viscous drag force terms of sand particles as well as SCBs, are shown as follows

138 (Dupont et al., 2013; Vinkovic et al., 2006):

139 $$\frac{\partial \tilde{u}_i}{\partial t} + \tilde{u}_j \frac{\partial \tilde{u}_i}{\partial x_j} = -\frac{1}{\overline{\rho}_f} \frac{\partial}{\partial x_i}(\tilde{p} - v\frac{\partial \overline{\rho}_f \tilde{u}_j}{\partial x_j}) - \frac{\partial \tau_{ij}}{\partial x_j} - \delta_{i3}g(\frac{\tilde{\theta}}{\overline{\theta}} - \frac{c_p}{c_v}\frac{\tilde{p}}{\overline{p}}) + \frac{F_i}{\overline{\rho}_f}, \tag{1}$$

140 where i = 1, 2 and 3 correspond to the streamwise, spanwise and wall-normal

141 directions (i.e., $x_1 = x$, $x_2 = y$, $x_3 = z$, $u_1 = u$, $u_2 = v$, $u_3 = w$), respectively; $\tilde{u}_i$, $\tilde{p}$ and

142 $\tilde{\theta}$ represent the filtered wind speed, pressure and potential temperature, respectively; v

143 is a damping coefficient of the attenuate acoustic waves; ρ_f is the air density; g is the

144 acceleration of gravity; $F_i = F_{pi} + F_{di}$ is the main feedback force, including the

145 feedback force provided by sand particles (F_{pi}, as shown in Section 2.2) and the SCBs

146 (F_{di}, as shown in Section 2.5); $\delta_{ij} = 1$ if $i = j$, otherwise $\delta_{ij} = 0$; $\tau_{ij} = \widetilde{u_i u_j} - \tilde{u}_i \tilde{u}_j$ are the

147 SGS (sub-grid-scale) stresses (Smagorinsky, 1963); c_p and c_v are the specific heat of

148 air at constant pressure and volume, respectively.

149 To solve above equations, the SGS stresses can be closed as follows:

150 $$\tau_{ij} - \frac{1}{3}\tau_{kk}\delta_{ij} = -(C_{sgs}\Delta)^2 \frac{1}{\sqrt{2}}\left|\frac{\partial \tilde{u}_i}{\partial x_j} + \frac{\partial \tilde{u}_j}{\partial x_i}\right|(\frac{\partial \tilde{u}_i}{\partial x_j} + \frac{\partial \tilde{u}_j}{\partial x_i}), \tag{2}$$

151 where Δ is the grid scale; C_{sgs} depends on the Germano subgrid-scale closure

152 method (Germano et al., 1991).

153   For the governing equations mentioned above, periodic boundary conditions are

154 applied for the spanwise direction. The upper and lower boundaries are set as a

155 stress-free condition and a rigid ground condition, respectively. The outlet boundary is

156 used as an open radiation condition in this paper. The inlet boundary is a given

157 logarithmic profile:

158 $\tilde{u}(0, \mathrm{y}, z) = (\dfrac{u_*}{\kappa}) \ln(\dfrac{z}{z_0}).$ (3)

159 Here k=0.41 is von Kármán constant; $z_0=d_{mean}/30$ is the aerodynamic surface

160 roughness (Kok et al., 2012), and d_{mean} is the mean diameter of the sand particles; u_*

161 is the friction speed of inflow. Additionally, the simulation is driven by a constant

162 flow corresponding to the given logarithmic wind profile. To accelerate the

163 development of boundary layer flow, the LWS method (Lund et al., 1998) is applied

164 to the inlet condition and the recycling plane at x_{ref}/Lx=12.5% (Inoue and Pullin,

165 2011). x_{ref} =5 m is the position of the recycling plane, and Lx=40 m is the total length

166 of the flow direction. The specific method reassigns the calculated mean velocity and

167 fluctuation at the recycling plane to the inlet at each fluid time step. A similar

168 application is described by Xu et al. (2018).

169 **2.2 Movement of the sand particles**

170   Saltating particles are moved by the drag force, gravity, electric field force,

171 Magnus force, Saffman force and so on (Murphy and Hooshiari, 1982). In our model,

172 the drag force and gravity are considered, ignoring other minor factors (Kok et al.,

173 2012; Zou et al., 2007). We employ the Lagrangian point-particle method to describe

174 particle motions, and the equations of particles with different sizes in three directions

175 can be expressed as

176 $m_p \dfrac{d^2x}{dt^2} = F_{px} = \dfrac{C_D \pi D^2 \rho_f}{8}(\tilde{u} - \dfrac{dx}{dt})^2 + F_{nx} + F_{sx},$ (4)

177 $m_p \dfrac{d^2y}{dt^2} = F_{py} = \dfrac{C_D \pi D^2 \rho_f}{8}(\tilde{v} - \dfrac{dy}{dt})^2 + F_{ny} + F_{sy},$ (5)

178 $m_p \dfrac{d^2z}{dt^2} = F_{pz} = -\dfrac{\pi g \rho_p D^3}{6} + \dfrac{C_D \pi D^2 \rho_f}{8}(\tilde{w} - \dfrac{dz}{dt})^2 + F_{nz} + F_{sz},$ (6)

179 where m_p is the mass of sand particles; $C_D = (0.63 + 4.8/\mathrm{Re}_p^{0.5})^2$ is the drag coefficient

180 of sand particles (Cheng, 1997). The particle Reynolds number can be expressed as

181 $\mathrm{Re}_p = (V_f \rho_p D / \mu)[(\tilde{u} - dx/dt)^2 + (\tilde{v} - dy/dt)^2 + (\tilde{w} - dz/dt)^2]^{1/2}.$ (7)

182 ρ_p and ρ_f are the density of sand particles and air, respectively; D is the diameter of

183 sand particles; $V_f = 1 - \sum\limits_{k=1}^{k=n} V_P / \Delta V$ is the bulk fraction which is the total sand volumes

184 within grid to the bulk of unit grid; ΔV is the bulk of unit grid; μ is the kinetic

185 viscosity coefficient of air; F_{nx}, F_{sx}, F_{ny}, F_{sy}, F_{nz} and F_{sz} are the normal and tangential

186 force of contact in three directions.

187 **2.3 Particle collision**

188   Modeling the collision process in the air among the ejection particles has been

189 the focus of previous studies (Carneiro et al., 2013; Huang et al., 2007). In this paper,

190 the "spring-damping model" is used to calculate the contact force when particles

191 collide in the air. The contact force can be described as follows (Huang et al., 2017):

192 The normal force of contact is

193 $$\vec{F}_{n,ij} = \begin{cases} -k_n \zeta_{n,ij}\, \vec{n}_{ij} - d_n\, \vec{v}_{n,ij} & , \quad \zeta = \left| R_i + R_j - \vec{r}_{ij} \right|, \\ 0 & , \quad \zeta < 0 \end{cases}$$ (8)

194 where $k_n = 2 \times 10^6$ is the normal stiffness coefficient; ζ is the amount of overlap

195 between particles during contact; R_i and R_j are the radius of particle i and j; $\vec{r}_{ij}$ is

196 distance vector between particles; $\vec{v}_{n,ij}$ is the normal relative velocity vector. The

197 normal damping coefficient can be expressed as

198 $$d_n = \sqrt{\frac{4 k_n \dfrac{m_i m_j}{m_i + m_j} (\ln \varepsilon)^2}{\pi^2 + (\ln \varepsilon)^2}},$$ (9)

199 where m_i and m_j are the mass of particle i and j, and $\varepsilon = 0.7$ is restitution coefficient.

200 The tangential force of contact is

201 $$\vec{F}_{t,ij} = \begin{cases} -k_t \zeta_{t,ij}\, \vec{\tau}_{ij} - d_t\, \vec{v}_{t,ij} & \left| \vec{F}_{t,ij} \right| \le \dfrac{R_i}{R_j} \left| \vec{F}_{n,ij} \right| \\ -\mu_i \left| \vec{F}_{n,ij} \right| \vec{\tau}_{ij} & \left| \vec{F}_{t,ij} \right| > \dfrac{R_i}{R_j} \left| \vec{F}_{n,ij} \right| \end{cases},$$ (10)

202 where $k_t = 2 \times 10^6$ is the tangential stiffness coefficient, $\zeta_{t,ij}$ is the tangential

203 displacement, and $\vec{v}_{t,ij}$ is the tangential relative velocity vector. The tangential

204 damping coefficient can be expressed as

205 $$d_t = 2 \sqrt{\frac{m_i m_j}{m_i + m_j} k_t}.$$ (11)

206 **2.4 Splash process**

207   Splash processes not only serve as an indispensable part of the near-surface

208 particle motions but also relate to the accuracy of emissions during particle upwards

209 transport. There are a large number of collisions between particles and the ground.

210   Meanwhile, other particles will be blown upwards when particles hit the ground,

211   which is referred to as the splash process. If energy-based collision analysis is

212   performed on a single particle, considerable time will be consumed. Therefore,

213   researchers have parameterized some key variables in accordance with the

214   characteristics of splashing, thereby simplifying the problem. We assume that there

215   are enough sand and dust particles on the ground to splash when the particles impact

216   the surface. If the particle collides with the bed, we assume the rebound probability as

217   $$p_{reb} = 0.95(1 - e^{-\lambda v_{imp}}),\tag{12}$$

218   where v_{imp} is the impact speed, and λ is an empirical parameter in the order of 2 s/m

219   according to the previous study (Anderson et al., 1991). The rebound sand speed is

220   0.55 times of the impact sand speed, and the rebound angle θ_{reb} is $40\,°$ (Zhou et al.,

221   2006). Of course, at a certain speed, some new sand particles will be splashed. The

222   ejection number is

223   $$\overline{N_{ej}} = n_0 \left(1 - \left(A - B\sin\theta_{imp}\right)^2\right) \left(\frac{v_{imp}}{\zeta\sqrt{gd_{mean}}} - 1\right)(e^{\mu_{imp}/C} - D),\tag{13}$$

224   where n_0=0.4, A=0.68, B=0.39, ζ=5, C=0.92, and D=1.39 (Huang et al., 2017). θ_{imp} is

225   the impact angle, μ_{imp} is the ratio of impact grain size to the mean size of the bed, and

226   d_{mean} is the mean diameter of the sand particles. The ejection angle θ_{ej} distributes

227   randomly between $50\,°$~$60\,°$ (Rice et al., 1995). The probability density distribution of

228   the initial lifting speed follows

229   $$p(v_{ej}) = \exp(-v_{ej} / \overline{v_{ej}}) / \overline{v_{ej}},\tag{14}$$

230 where v_{ej} is the ejection speed and the overbar represents a mean value (Anderson et

231 al., 1991; Werner, 1990). The mean ejection speed can be expressed as (Kok and

232 Renno, 2009)

233 $$\overline{v_{ej}} = \sqrt{gD_{mean}}\frac{\alpha_{ej}}{a}(1-\exp(-\frac{v_{imp}}{40\sqrt{gD_{mean}}})).$$ (15)

234 Moreover, the sand particles satisfy the periodic boundary condition in the streamwise

235 and spanwise directions. Following the idea of Dupont et al. (2013), aerodynamic

236 entrainment is not considered in our model. A total of 10000 initial particles are

237 randomly released in the flow field (Huang, 2020), and the release height should be

238 lower than 0.3 m (Shao and Raupach, 1992). The results of Dupont et al. (2013)

239 showed that the number of released particles does not affect the final results but only

240 the speed of wind-blown sand development.

241 **2.5 Parameters and the equivalent method of SCBs**

242 According to the experience of laying SCBs in practical engineering (Chang et

243 al., 2000) and the theoretical results of Wang and Zheng (2002), in this paper, the

244 height of the SCB (S_h) is set to 10 cm, the side length of a single SCB (S_l) is set to 100

245 cm, and the side thickness of the SCB (S_n) is set to 10 cm. The diagram of a single

246 SCB is shown in Fig. 1b. Moreover, to study the inhibition effect of the laying length

247 of SCBs (represented by N) on aeolian sand erosion, we set N=5~10 m, 5~20 m, and

248 5~30 m in the simulation cases. The diagram of the laying SCBs is shown in Fig. 1a,

249 and the main parameters of the SCBs are listed in Table 1.
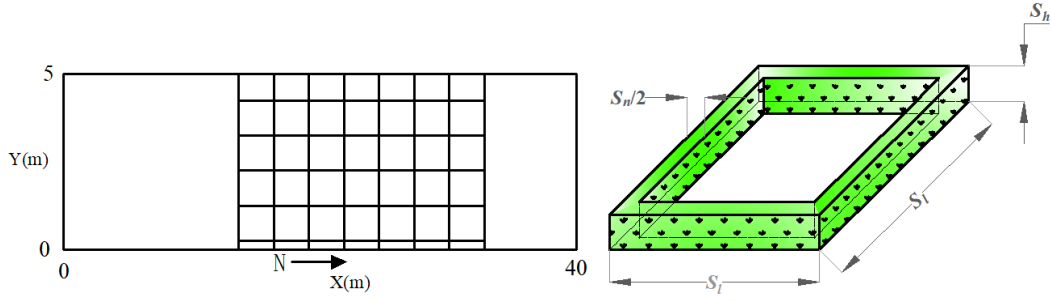
Figure 1. (a) The diagram of the laying SCBs. (b) The diagram of a single SCB.

The SCBs are equivalent to a volume resistance force through the resistance coefficient and leaf area coefficient; that is, the flow in these regions will be subject to an additional resistance force, which can be expressed as

$$F_{di} = -C_d a_d |U| u_i, \tag{16}$$

where C_d is the drag coefficient, a_d is the leaf area coefficient, and U is the inflow wind speed. In the simulation, the value of C_d is 0.2 according to the parameters of Dupont et al. (2013). Nepf (2012) concluded that when the diameter of vegetation is 4-9 cm, the value of the leaf area coefficient a can reach 20 m^{-1}. Therefore, according to the side thickness of the SCB presented in this paper, the leaf area coefficient is set as 40 m^{-1}. Due to the limitation of the drag force method, the SCBs only affect the velocity of the flow field rather than the real presence. Current model considers more the inhibition effect of the flow field on the particles and does not simulate the collision process between the sand particles and the SCBs. Therefore, this collision-obstruction process can be approximately simplified as the sudden drop in the drag force as the saltating particles pass through the region of the SCBs. The consequences of such a simplification may lead to an underestimation of the inhibition effect of the SCBs. Therefore, this limitation of the current model needs to be noted.

270 **Table 1** SCB Parameters

Name	Symbol	Value	Unit
SCB height	S_h	10	cm
SCB side length	S_l	100	cm
SCB side thickness	S_n	10	cm
laying length of SCBs	N	5~10, 5~20, 5~30	m
drag coefficient	C_d	0.2	
leaf area coefficient	a	40	m^{-1}

271

272 **2.6 Calculation parameters**
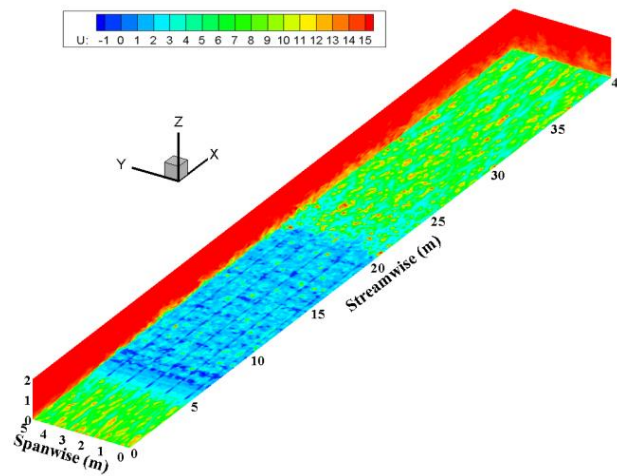
273
274 **Figure 2.** Schematic diagram of three-dimensional wind-blown sand in presence of SCBs.

275   Wind tunnel experiments conducted by Shao and Raupach (1992) indicated that

276 a complete "overshoot" was more than 10 m in streamwise (Huang et al., 2014; Ma

277 and Zheng, 2011). In Fig. 2, the computational domains are Lx=40 m, Ly=5 m, and

278 Lz=2 m in the streamwise, spanwise and wall-normal directions, respectively. Field

279 experiments conducted by Baas and Sherman (2005) showed that the mean lateral size

280 of sand streamers is approximately 0.2 m. To capture this structure, the mesh spacing

281 is N_x=0.1 m and N_y=0.05 m in the streamwise and spanwise directions, respectively.

282 In addition, in the near-wall region, logarithmic stretching has been adopted to ensure

283 precision. The mean and minimum mesh spacing in the vertical direction is N_z=0.025

284   m and N_{zmin}=0.005 m, respectively. Therefore, the grids of the streamwise, spanwise

285   and vertical directions are 400×100×80, respectively. The sand particle diameter

286   satisfies the normal distribution: the mean diameter equals 200 μm, and the variance

287   is ln(1.2). We first simulate the clean air field flow in the presence of SCBs for 30

288   seconds to obtain the full development of the flow field. Then, we add sand particles

289   to the flow field to obtain a sand-laden flow. After the wind-blown sand flow becomes

290   saturated, the simulations continue for another 20 seconds to perform the statistics.

291   The fluid time step is Δt_s=0.0002 s, and the particle time step is Δt_p=0.00005 s. The

292   sand grain density is 2650 kg/m^3, and the air density is 1.225 kg/m^3. The main

293   calculation parameters are listed in Table 2.

294

295   **Table 2** Main Simulation Parameters

Name	Symbol	Value	Unit
streamwise computational domain	Lx	40	m
spanwise computational domain	Ly	5	m
wall-normal computational domain	Lz	2	m
fluid time step	Δt_s	0.0002	s
friction wind speed	u_*	0.3, 0.44, 0.6	m/s
particle time step	Δt_p	0.00005	s
sand density	ρ_a	2650	kg/m^3
air density	ρ_f	1.225	kg/m^3
gravity	g	9.81	m/s^2
streamwise mesh spacing	N_x	0.1	m
spanwise mesh spacing	N_y	0.1	m
wall-normal mean mesh spacing	N_z	0.025	m

296

3. Model validations

3.1 Particle field validation

299
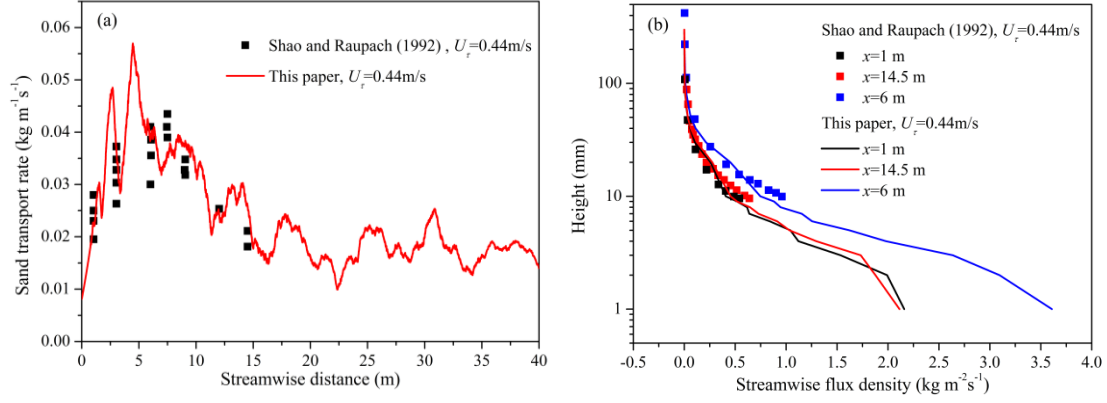
Figure 3. (a) The spatial variation of the streamwise sand transport rate in the sand-laden flow. (b)
The streamwise sand transport rate density with the height at the three flow direction positions.

In section 3.1, we will verify the validity of the model from the following two

aspects. The sand transport rate is an important physical quantity in wind-blown sand,

which is the embodiment of the sediment carrying capacity of the flow field (Zheng,

2009). Therefore, without considering the SCBs, we first compare the spatial variation

in the sand transport rate in the sand-laden flow with the experimental results of Shao

and Raupach (1992). The sand transport rate is calculated according to the formula

$$q(x) = \sum_{z=0}^{z=Lx} \sum_{y=0}^{y=Ly} m(x, y, z) \, / \, \Delta x \, / \, \Delta t_s, \qquad (17)$$

where $m(x, y, z)$ represents the sand mass, and Δx is the grid size in the flow direction.

Whether the wind-blown sand flow is saturated depends on the change in sediment

transport at a certain streamwise position. The condition for judging saturation is

given by Ma and Zheng (2010). The wind tunnel experimental results of Shao and

Raupach (1992) showed that the streamwise sand transport rate first increased and

then decreased until it was stable, which is called the "overshoot" phenomenon

(Anderson and Haff, 1991; McEwan and Willetts, 1991). Fig. 3a shows the

comparison between the simulation results of the sand transport rate along the flow

direction and the experimental results of Shao and Raupach (1992) under the same

friction wind speed. As shown in Fig. 3a, our simulation results also show this

phenomenon. However, unlike the other numerical simulation results (Huang et al.,

2014; Ma and Zheng, 2011), our sediment transport rate results have an obvious

fluctuation characteristic and are not smooth curves, which may be caused by the

turbulence intermittency unique to the three-dimensional wind-blown sand model.

Moreover, we give the distribution results of the streamwise sand transport rate

density with the height at the three flow direction positions, which are compared with

the experimental results. From Fig. 3b, we can see that the distribution of the

streamwise sand transport rate density with height follows the trend of exponential

decline, and the sand transport rate density at $x = 6$ m is significantly higher than that

at $x = 1$ m and $x = 14.5$ m, which is consistent with the experimental results of Shao

and Raupach (1992). This is because the streamwise position of $x = 6$ m is in the peak

region of the "overshoot" phenomenon, while the streamwise positions of $x = 1$ m and

$x = 14.5$ m are in the rising region and stable region, respectively. Due to the massive

accumulation of sand particles near the surface (0-20 mm), the concentrations cannot

be easily measured. In Fig. 3b, our simulation results also show that the distribution of

the streamwise sand transport rate density with heights below 10 mm still satisfies the

trend of exponential decline. However, at a height of 2~3 mm, there is a slight change

in this trend; that is, the rate of increase in the sand transport rate density slows down,

which is not revealed in the experimental results. Due to the limitations of the large

eddy simulation, the simulation results near the wall may be distorted and requires

339 further experimental verification.
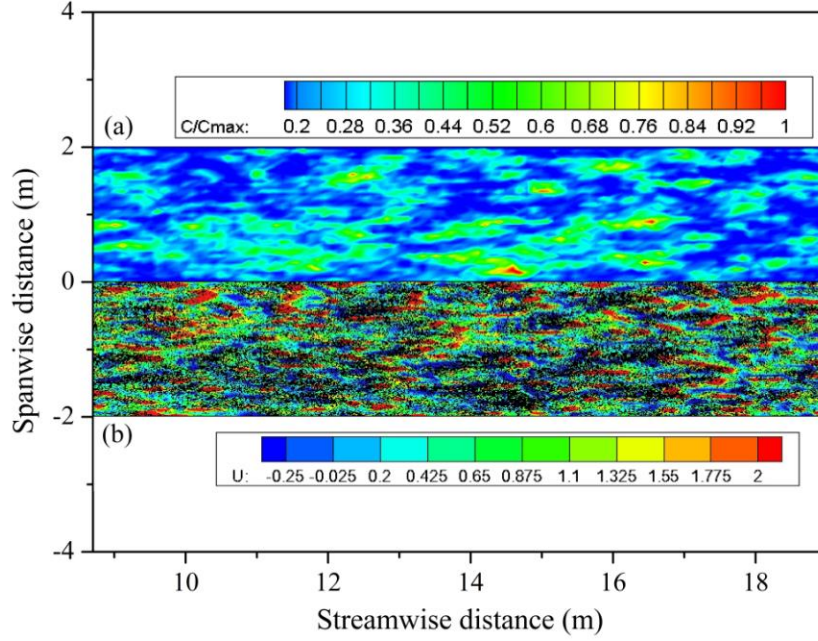
340

341 **Figure 4.** (a) The top view of the sand streamer concentrations, where C represents the particle
342 concentrations, C_{max} represents the maximum particle concentrations. (b) The top view of the
343 whole particle positions and the streamwise velocity diagram of flow field with the height of 0.005
344 m, and the y coordinates are correspondingly shifted down by 2, where the black dots represent
345 the sand particles, U represents the streamwise wind speed of the sand-laden flow (u_τ=0.3 m/s).

346 Sand streamers, as a natural phenomenon in wind-blown sand, have been widely

347 studied. Therefore, without considering the SCBs, we analyse the morphology of the

348 sand streamer and its relationship with the flow field. In the meantime, the airborne

349 particle concentration within a certain area can be calculated as

350
$$C = \sum_{z=0}^{z=Lz} \sum_{y=0}^{y=Ly} \sum_{x=0}^{x=Lx} m(x, y, z) / Lx / Ly / Lz. \tag{18}$$

351 Fig. 4a shows the top view of the particle-aggregation morphology in the stable stage

352 of sand-laden flow. It can be seen from Fig. 4a that the concentration of sand particles

353 is intermittent in both streamwise and spanwise directions. Moreover, we can see

354 clearly that the morphological characteristics of the sand streamer are consistent with

355   the observations of Baas and Sherman (2005), that is, it is up to a few metres in the

356   streamwise direction and approximately 0.2 metres in the spanwise direction. Our

357   model can sufficiently reproduce the "sand streamer" phenomenon in wind-blown

358   sand. Here, we need to point out that the intermittence of turbulence complicates

359   particle movement, especially when multiple streamers are connected end to end and

360   the concentration is sufficiently close, and then super sand streamers up to tens of

361   metres long will exist. Whether in sand-laden flow or other two-phase flows,

362   researchers are generally concerned about the aggregation of particles. We plot the

363   position of particles and the streamwise velocity of the flow field in Fig. 4b and find

364   that most particles are assembled in the low-speed streaks, which is consistent with

365   the conclusion of the other particle-laden flow studies (Lee and Lee, 2015; Richter,

366   2015).

367   **3.2 Velocity field validation**

368
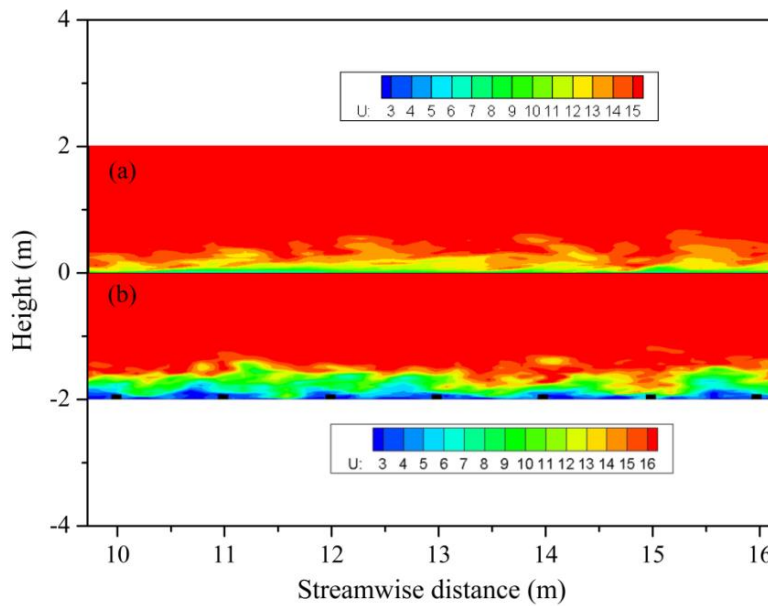
369   **Figure 5.** The side view of X-Z plane streamwise velocity before (a) and after (b) containing the

370   SCBs (u_τ=0.6 m/s, N=5~20 m, y=0 m). The y coordinates are correspondingly shifted down by 2

371   in the case (b).

372

373
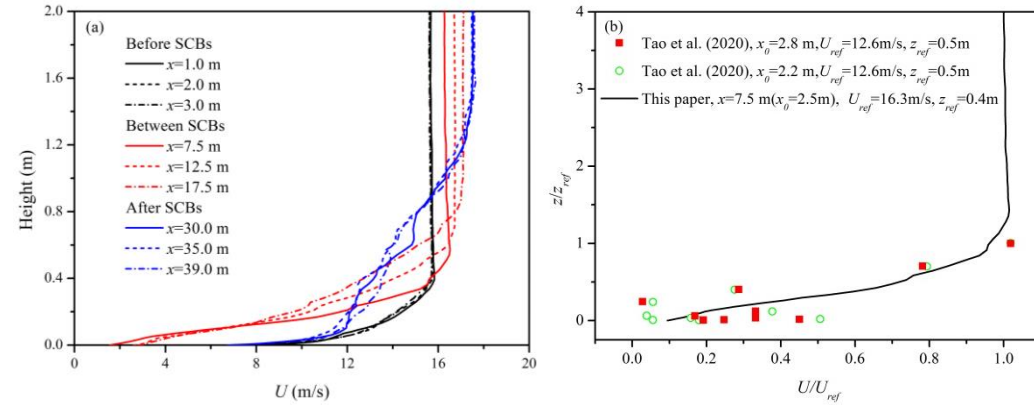
374   **Figure 6. (a)** The wind speed profiles of different streamwise positions in the clean air flow

375   containing the SCBs (u_τ=0.6 m/s, N=5~20 m); (b) The dimensionless wind speed varying with

376   dimensionless height, comparison between our simulated results and the existing experiment.

377   The verification of the flow field part of the program is covered in detail in our

378   previous works (Huang, 2020). In section 3.2, we focus on the flow field verification

379   after considering the SCBs. We verify the difference in the velocity profile as well as

380   the surface roughness in the clean air flow with and without the SCBs.

381   In previous work, the wind speed and surface roughness near the SCBs were well

382   studied (Dong et al., 2000; Qu et al., 2007; Wang et al., 1999). These works all

383   pointed out that laying the SCBs can effectively increase the surface roughness and

384   reduce the wind speed near the surface to play a role in inhibiting the wind-blown

385   sand and fixing the sand particles. Fig. 5a and 5b are the tangent plane (X-Z plane) of

386   the streamwise wind velocity without and with the SCBs, respectively. It can be seen

387   intuitively that the existence of the SCBs significantly reduces the surface wind speed

388   and increases the boundary layer thickness of the flow field. To reveal the difference

389   quantitatively, we plot the wind speed profiles of different streamwise positions in the

390   clean air flow containing the SCBs in Fig. 6a. The selected positions are x = 1, 2, and

391   3 m in front of the SCBs, x = 7.5, 12.5, and 17.5 m in the area containing the SCBs,

392 and $x = 30$, 35, and 39 m behind the SCBs. We can see that the wind speed profiles at

393 the three positions in front of the SCBs are basically the same. In the area containing

394 the SCBs, the existence of the SCBs reduces the surface wind speed and increases the

395 thickness of the boundary layer (equivalent to increasing the surface roughness) as

396 well as the incoming wind speed outside the boundary layer. Moreover, the longer the

397 SCBs are, the thicker the boundary layer becomes, and the incoming wind speed

398 outside the boundary layer will also increase. The flow field behind the SCBs may be

399 complicated by the influence of the attached vortex generated by the SCBs, but the

400 overall trend is the same, and the boundary layer thickness remains consistent. These

401 results are qualitatively consistent with the conclusions of previous work (Dong et al.,

402 2000; Qu et al., 2007; Wang et al., 1999), which indicates that our model has

403 effectively introduced the SCB module.

404   In addition, we compared the wind speed profiles with the experimental results

405 of Tao et al. (2020). In Figure 6b, the streamwise wind speed in the horizontal

406 coordinate is dimensionless with the reference wind speed U_{ref} and the height in the

407 vertical coordinate is dimensionless with the reference height z_{ref}. In the wind tunnel

408 experiment conducted by Tao et al. (2020), the maximum boundary layer thickness is

409 given as 0.5 m, so the reference height is taken as z_{ref}=0.5 m. Then, the wind speed at

410 z=0.5 m is determined as the reference wind speed U_{ref}=12.58 m/s based on their inlet

411 wind profiles. In our simulation case, z_{ref}=0.4 m is the initial inlet boundary layer

412 thickness, and U_{ref}=16.3 m/s is the reference wind speed. We select the experimental

413 results of wind speed profiles at the SCB belt positions x_0=2.2 m and 2.8 m along the

414 flow direction to compare with our numerical results at x_0=2.5 m (streamwise position

415 x=7.5 m). The dimensionless results show that our results are consistent with the

416 experimental results in quantitative and qualitative, which indicates that our model

417 can well reveal the inhibition effect of SCBs on the flow field. In the following

418 section, we will reveal more about the influence of the laying length on the wind field

419 and its inhibition effect on wind-blown sand.

420

4. Results and discussion

4.1 Influence of the SCBs on the clean air flow
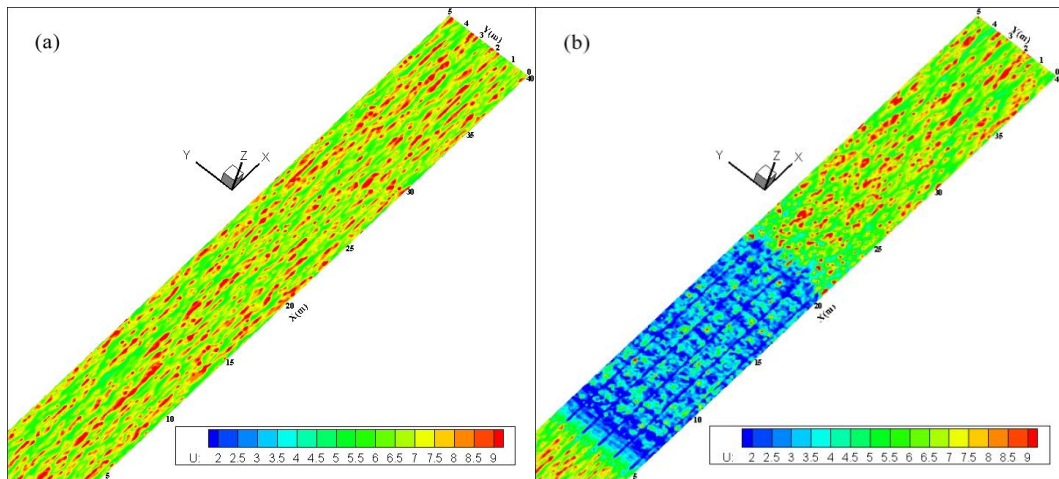
Figure 7. The top view of X-Y plane streamwise velocity without (a) and with (b) the SCBs
(z=0.005 m, u_τ=0.6 m/s, N=5~20 m).
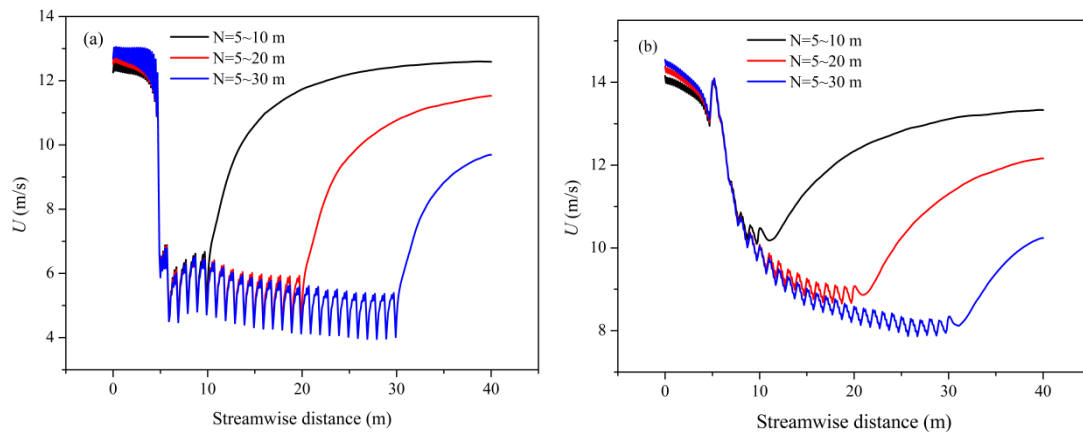
Fig. 7a and 7b show that the presence of the SCBs destroys the original streaks of the clean air flow and decreases the wind speed. In most cases, the wind speed in the central area of a single SCB is significantly higher than that in the surrounding area, showing a block of velocity distribution characteristics. Although the wind speed behind the SCBs will recover rapidly, there is a significant difference between the newly formed streaks and the original streaks of the flow field; that is, the streamwise scale of the streaks behind the SCBs is significantly shorter than before. The variation in streamwise wind speed at the different laying length cases (N=5~10 m, 5~20 m, 5~30 m) under the same friction wind speed (u_τ=0.6 m/s) is plotted in Fig. 8, where Fig. 8a corresponds to the wind speed at a height of 0.1 m, and Fig. 8b corresponds to the wind speed at a height of 0.2 m. Fig. 8 shows an oscillating decrease in wind speed in the SCBs. In addition, behind the SCBs, the wind speed gradually increases and then stabilizes. The trend of wind speed reduction in the SCBs is consistent with the existing experimental results (Xu et al., 1982). The difference is that the reduction process of the wind speed around the SCBs exhibited an oscillatory attenuation instead of a continuous decrease, which was not revealed in the previous simulation results (Bo et al., 2015). Moreover, when the incoming wind speed is stable, the longer the laying lengths are, the lower the wind speed in the stable stage behind the SCBs will be. This is very useful information. On this basis, we can obtain the relationship between the laying length of the SCBs and the wind speed in the stable stage according to an actual situation. For example, the wind speed in the stable stage

451 can be reduced to the impact threshold or the aerodynamic threshold on both sides of

452 the desert highway to determine the minimum laying length of the SCBs and save

453 laying costs. This is a potential application of our model and needs further

454 experimental verification.

455

456 **4.2 Effect of sand particles on the flow field and its aggregation location**

457
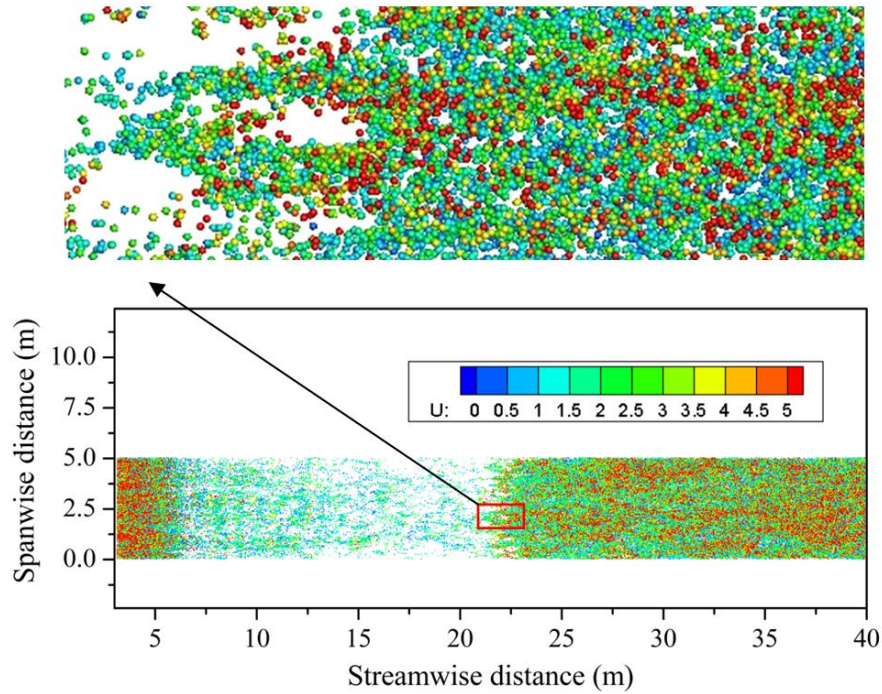
458 **Figure 9.** The top view of the particle positions of the wind-blown sand in presence of SCBs,
459 where U represents the speed of the particles (u_τ=0.6 m/s, N=5~20 m).
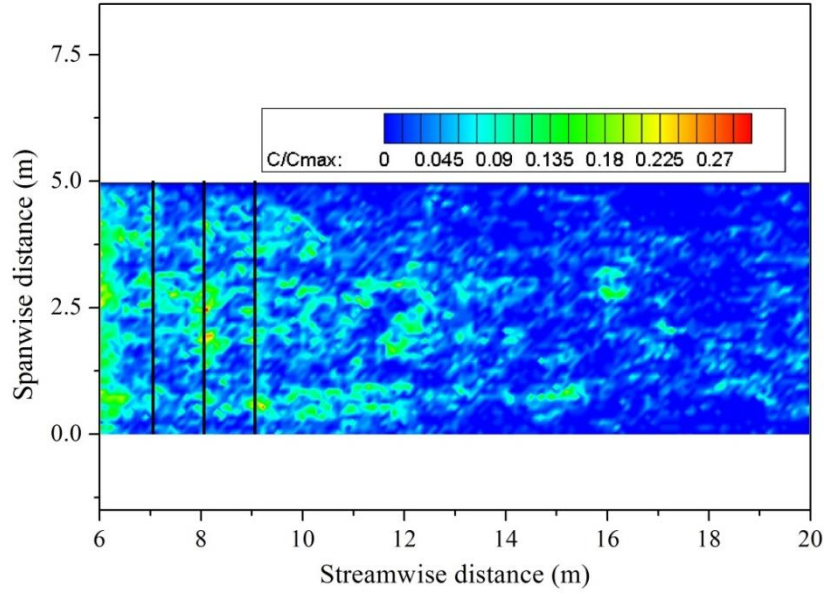
Figure 10. The top view of the sand concentrations in the regions of the SCBs, where C represents the particle concentrations, C_{max} represents the maximum particle concentrations (u_τ=0.6 m/s, N=5~20 m). The black lines represent the schematic diagram of the side of SCBs.

Sand particles were added to the clean air flow field in the presence of SCBs to fully develop and reach stability. The top view of the particle positions of the wind-blown sand after reaching a stable state is shown in Fig. 9. From Fig. 9, we can see that when the wind-blown sand passes through the SCBs, the particle number obviously decreases gradually, and the inhibition effect of the SCBs on the wind-blown sand can be visualized. Moreover, the motion of sand particles behind the SCBs returns to complete wind-blown sand movement. We then plot the sand concentrations of the region in the presence of SCBs in Fig. 10. Combining the laying position of the SCBs as well as the corresponding sand concentrations, we can clearly see that the concentration of sand particles near the side of the SCBs is higher than that in its central region, which is consistent with the conclusion of Xu et al. (2018). On the one hand, the wind speed near the side of SCBs is low, and the drag force of the sand particles in these areas will be significantly reduced, so that the sand particles

477   will accumulate or deposit in these regions. On the other hand, the wind speed in the

478   central area of every single SCB is significantly higher than that in the surrounding

479   area, so sand particles do not easily accumulate or fall in these regions. This explains

480   why the side of the SCBs tends to be buried in sandy land and loses its effect after

481   long working hours.

482

483
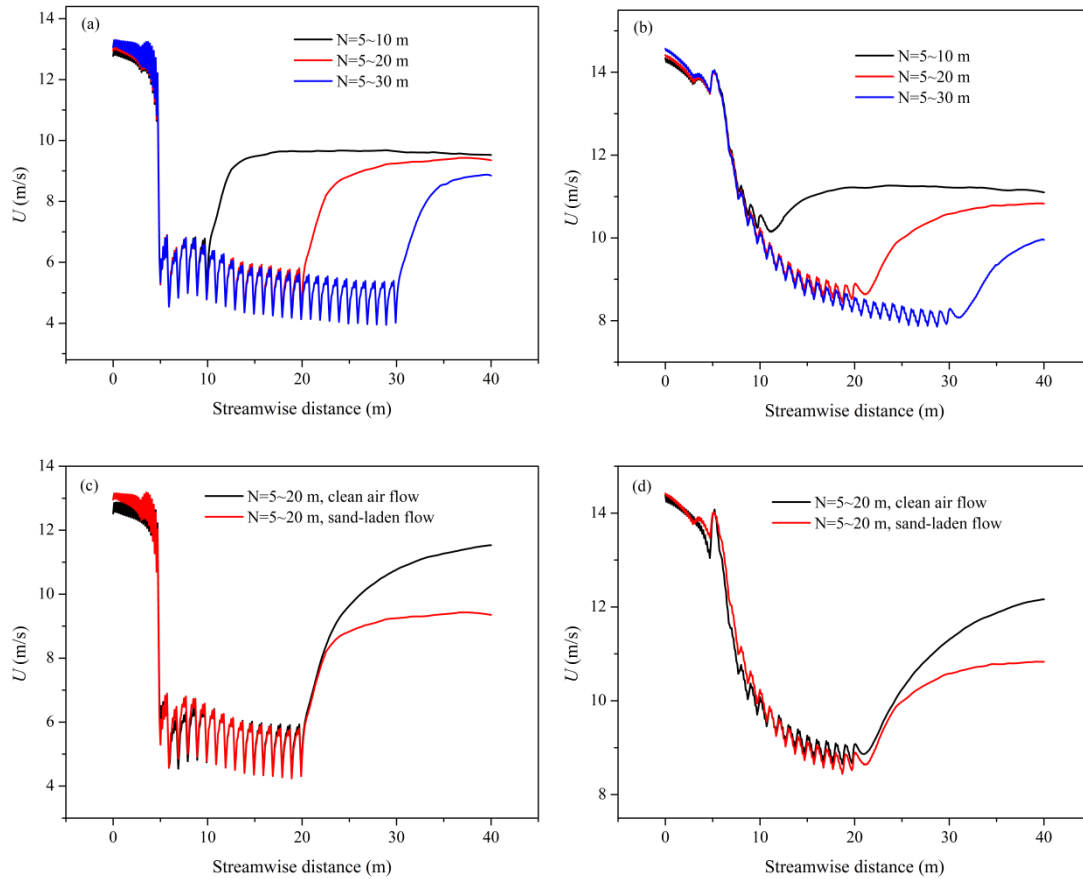
484 **Figure 11.** The streamwise wind speed in the sand-laden flow containing the SCBs at the height of
485 0.1 m (a) and the height of 0.2 m (b), u_τ=0.6 m/s, N=5~10 m, 5~20 m, 5~30 m. The comparison of
486 the streamwise wind speed between the clean air flow and the sand-laden flow at the height of 0.1
487 m (c) and the height of 0.2 m (d), u_τ=0.6 m/s, N=5~20 m.

488   Furthermore, we analyse the effect of sand particles on the wind speed in the

489   sand-laden flow. The streamwise wind speed of the sand-laden flow at the different

490   laying length cases (N=5~10 m, 5~20 m, 5~30 m) under the same friction wind speed

491   is plotted in Fig. 11a and 11b. Meanwhile, for the convenience of comparison, the

492 streamwise wind speed under the same laying length (N=5~20 m) in the sand-laden

493 flow and the clean air flow are plotted in Fig. 11c and 11d. Fig. 11a and 11c

494 correspond to the wind speed at a height of 0.1 m, while Fig. 11b and 11d correspond

495 to the wind speed at a height of 0.2 m. From Fig. 11a-d, we can still see an oscillating

496 decrease in the wind speed in the SCBs of the sand-laden. The streamwise wind speed

497 behind the SCBs in the sand-laden flow is significantly lower than that in the clean air

498 flow. Obviously, the presence of sand particles indeed reduces the wind speed.

499 However, the change in wind speed in the SCBs between the sand-laden flow and the

500 clean air flow is not obvious because there are fewer sand particles in the SCBs than

501 behind the SCBs, which has less effect on the overall wind speed.

502 **4.3 Effect of the laying length on the sand transport rate**

503
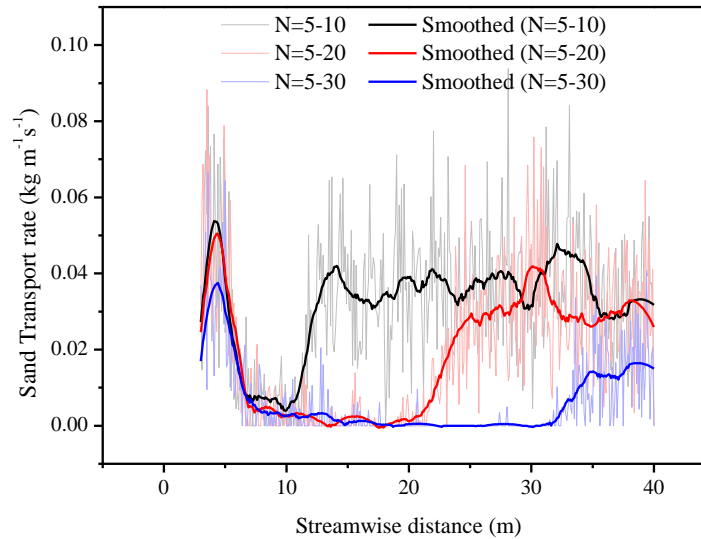
504 **Figure 12.** The streamwise sand transport rate in the different laying length cases (u_τ=0.6 m/s,

505 N=5~10 m, 5~20 m, 5~30 m). Dark lines are the result of smoothing.

506   The effect of the different laying length cases (N=5~10 m, 5~20 m, 5~30 m) on

507 the sand transport rate under the same friction wind speed is plotted in Fig. 12. It can

be seen from Fig. 12 that the sand transport rate in the SCBs is very low, and as the

laying length increases, the sand transport rate in the SCBs decreases. In the case of

N=5~30 m, the sand transport rate in some regions has been reduced to zero.

Therefore, this result once again shows that the laying length of the SCBs can be

optimized, and we can reduce the laying cost while maintaining the effect of the SCBs.

Especially on both sides of the desert highway, our model can give the minimum

laying length according to the actual parameters. At the same time, we notice that the

sand transport rate will increase rapidly and then reach a stable state behind the SCBs.

It is obvious that when N=5~30 m, the value of the sand transport rate at the stable

stage behind the SCBs is significantly lower than the other results of N=5~10 m and

N=5~20 m. We also notice that the longer the laying lengths are, the lower the sand

transport rate in the stable stage behind the SCBs will be. This result corresponds to

the result shown in Fig. 8. Our results indicate that when sandy land is wide, the

discontinuous laying method can be considered. That is, the minimum laying length

must be determined first, and then the distance between each minimum laying length

can be set as needed. In this way, the sand transport rate can be reduced in sections.

This is another potential application of our model.

4.4 Particle positions under different friction wind speeds

526
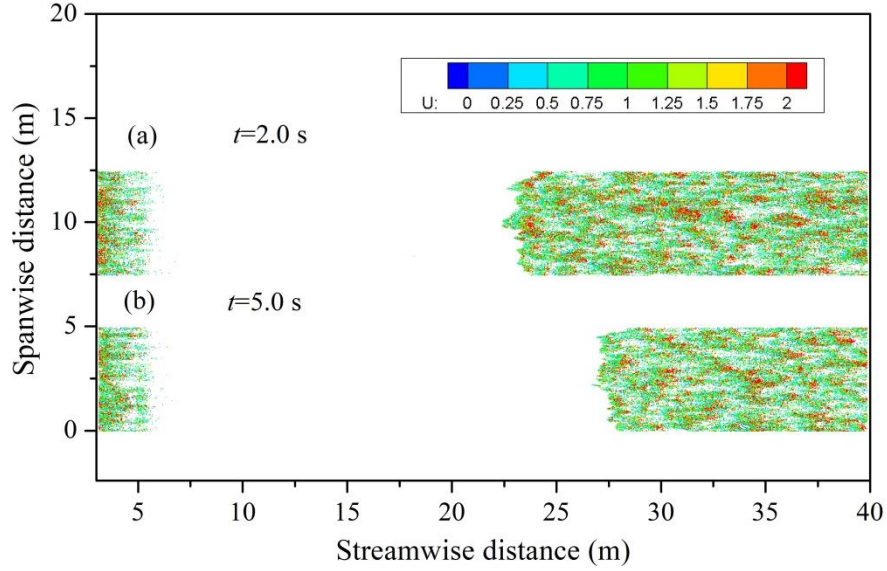
Figure 13. The top view of the particle positions of the wind-blown sand in presence of SCBs at the time t=2.0 s (a) and t=5.0 s (b), where U represents the speed of the particles (u_τ=0.3 m/s, N=5~20 m). The y coordinates are correspondingly shifted up by 7.5 per case.

530
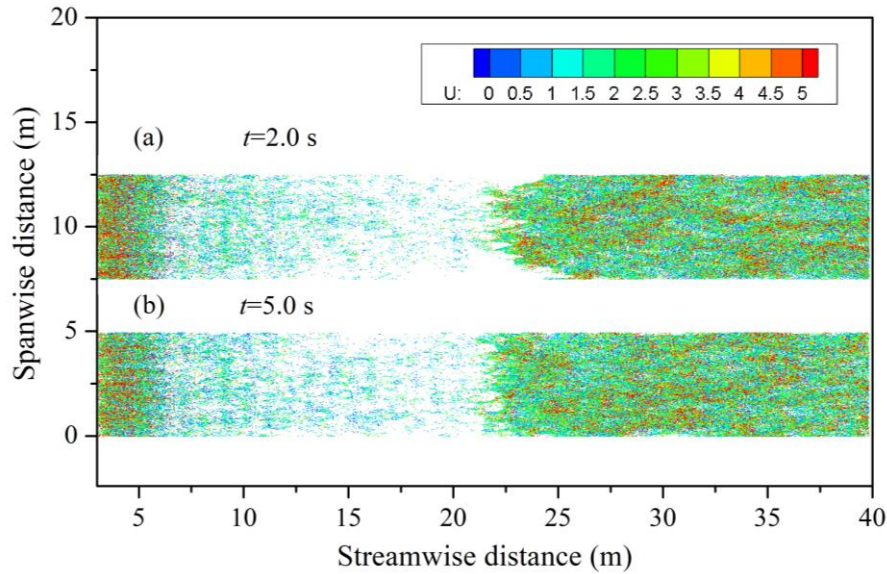
Figure 14. The top view of the particle positions of the wind-blown sand in presence of SCBs at the time t=2.0 s (a) and t=5.0 s (b), where U represents the speed of the particles (u_τ=0.6 m/s, N=5~20 m). The y coordinates are correspondingly shifted up by 7.5 per case.

The above analysis is based on the calculation case when the friction wind speed

is 0.6 m/s, and the sand particles can easily penetrate the SCBs when the wind speed

is large. When the friction wind speed is small, the inhibition effect of the SCBs on

wind-blown sand will become more obvious, and the movement behaviour of sand

538 particles will change. We focused on the effect of SCBs on the wind-blown sand

539 within 2 to 5 seconds after the sand-laden flow is saturated. We plot the top view of

540 the particle positions at different moments (t=2 s, 5 s) when the friction wind speed is

541 0.3 m/s and 0.6 m/s in Fig. 13 and Fig. 14, respectively. The initial value of time t in

542 Fig. 13 and Fig. 14 is when sand particles are added. The results show that when the

543 wind speed is small, the sand particles cannot penetrate the SCBs. There is no obvious

544 sand movement in the SCBs, and stable wind-blown sand cannot be formed behind

545 the SCBs. With the passage of time, the wind-blown sand behind the SCBs gradually

546 disappears. It is worth noting that aerodynamic entrainment is not considered in our

547 model. This is a considerable limitation of our model in the simulation of wind

548 erosion in the presence of SCBs. Therefore, a more reasonable situation is that when

549 the wind speed behind the SCBs returns to the fluid threshold, this part of the

550 wind-blown sand should still develop. When the wind speed is relatively small, on the

551 one hand, the sand particles cannot completely penetrate the regions of the SCBs and

552 cannot continuously provide the impact particles to form the wind-blown sand behind

553 the SCBs. On the other hand, the SCBs affect the surface wind speed behind it, thus

554 also affecting the continuous formation of wind-blown sand. When the wind speed is

555 relatively high, the sand particles can penetrate the SCBs. With increasing laying

556 length, although the inhibition effect on wind-blown sand is more obvious, stable

557 wind-blown sand will still be formed behind the SCBs. We think that when the laying

558 length of the SCBs is fixed, whether the wind speed will decrease below the impact

559 threshold or the fluid threshold is the key to determining whether the sand particles

can penetrate the SCBs and form stable wind-blown sand behind the SCBs. To present

this phenomenon more clearly, we have animated this process, as shown in the

supplementary materials (Video 1 and Video 2). In actual anti-desertification projects,

the minimum laying length of the SCBs can be determined by our model according to

the local maximum friction wind speed.

5. Conclusion and outlook

In this paper, a three-dimensional wind-blown sand coupling model in the

presence of SCBs was established. The model was verified from the following aspects:

(1) spatial distribution of the sand transport rate; (2) morphological characteristics of

the sand streamer resulting from the instantaneous fields; and (3) changes in the

thickness of the boundary layer before and after the SCBs. From this model, the

inhibition effect of SCBs on wind-blown sand was studied qualitatively, and the

sensitivity of aeolian sand erosion to the laying length was investigated. The results

showed that the wind speed in the SCBs of the clean air flow or the sand-laden flow

both decreases in an oscillating manner, which has not been revealed by previous

studies. Moreover, the longer the laying lengths of the SCBs are, the lower the wind

speed and the sand transport rate in the stable stage behind the SCBs will be, which

may provide theoretical support for the minimum laying length of SCBs in

anti-desertification projects. More importantly, we found that the concentration of

sand particles near the side of SCBs is higher than that in its central region, which is

consistent with previous research. This explains why the boundary of the SCBs tends

to be buried in sandy land and loses its effect after long working hours. Our results

also indicated that whether the wind speed will decrease below the impact threshold

or the fluid threshold is the key factor affecting whether sand particles can penetrate

the SCBs and form stable wind-blown sand behind the SCBs under the same

conditions. Although our model has been able to reveal the inhibition effect of the

SCBs on wind-blown sand, there are still some aspects that need improvement, such

as aerodynamic entrainment, particle deposition on the SCB, and collision between

the sand particles and the SCBs. The resolution of these issues is expected to reveal

more details of particle deposition around the SCBs, which needs in-depth study. The

size of the SCB used in our model is fixed. In future work, we plan to analyse the

effect of different heights and widths of the SCB on aeolian sand erosion and discuss

the reasons for the difference in heights between the SCB and other obstacles, such as

sand fences. Another aspect worth noting is that some additional factors, such as

terrain and surface roughness, will affect SCB performance in anti-desertification

projects, so the influence of these factors should be considered in the future. Using the

proposed model, our work significantly analysed some results that are seemingly

simple but lack a theoretical basis from the perspective of turbulence.

Acknowledgments

This research was supported by grants from the National Natural Science Foundation

of China (Grant number 12002119), Opening Foundation of MOE Engineering

Research Center of Desertification and Blown-sand Control, Beijing Normal

University (2021-B-4). The author expresses sincere appreciation to the supports. The

author would like to thank the Center for Analysis and Prediction of Storms (CAPS)

at the University of Oklahoma for providing the original ARPS code. And I am also

thankful to Editor Andreas Baas for his careful help with the manuscript and to Dr.

Catherine Le Ribault and another anonymous reviewer for their helpful comments.

Code and Data availability. All relevant code and data used to generate the

figures in this paper can be accessed using the following email: hjhuang@usst.edu.cn.

Competing interests. The authors declare that there are no competing interests

Author contributions. HJ performed the programming, analyzed the results, and

wrote the paper.

Video supplement. Video 1 and Video 2 can be downloaded at the following link:

https://doi.org/10.5281/zenodo.6937805

References

Anderson, R. S. and Haff, P.: Wind modification and bed response during saltation of sand in air, Acta Mech. Supp. 1, 21-51, 1991.

Anderson, R. S., Sørensen, M., and Willetts, B. B.: A review of recent progress in our understanding of aeolian sediment transport, Acta Mech. Supp. 1, 1-19, 1991.

Baas, A. C. W. and Sherman, D.: Formation and behavior of aeolian streamers, J. Geophys. Res. Earth Surf. 110(F3) , 2005.

Bitog, J., Lee, I. B., Shin, M. H., Hong, S. W., Hwang, H. S., Seo, I. H., Yoo, J. I., Kwon, K. S., Kim, Y. H., and Han, J. W.: Numerical simulation of an array of fences in Saemangeum reclaimed land, Atmos. Environ. 43(30), 4612-4621, 2009.

Bo, T. L., Ma, P., and Zheng, X. J.: Numerical study on the effect of semi-buried straw checkerboard sand barriers belt on the wind speed, Aeolian Res. 16, 101-107, 2015.

Bouvet, T., Wilson, J., and Tuzet, A.: Observations and modeling of heavy particle deposition in a windbreak flow, J. Appl. Meteorol. Climatol. 45(9), 1332-1349, 2006.

Carneiro, M. V., Araújo, N. A., Pähtz, T., and Herrmann, H. J.: Midair collisions enhance saltation, Phys. Rev. Lett. 111(5), 058001, 2013.

Chang, Z., Zhong, S., Han, F., and Liu, H.: Research of the suitable row spacing on clay barriers

and straw barriers, J. Desert Res. 20(4), 455-457, 2000.

Chen, B., Cheng, J., Xin, L., and Wang, R.: Effectiveness of hole plate-type sand barriers in reducing aeolian sediment flux: Evaluation of effect of hole size, Aeolian Res. 38, 1-12, 2019.

Cheng, J. J. and Xue, C. X.: The sand-damage-prevention engineering system for the railway in the desert region of the Qinghai-Tibet plateau, J. Wind Eng. Ind. Aerodyn. 125, 30-37, 2014.

Cheng, J. J., Lei, J. Q., Li, S. Y., and Wang, H. F.: Disturbance of the inclined inserting-type sand fence to wind-sand flow fields and its sand control characteristics, Aeolian Res. 21, 139-150, 2016.

Cheng, N. S.: Simplified settling velocity formula for sediment particle, J. Hydraul. Eng. 123(2), 149-152, 1997.

Dai, Y., Dong, Z., Li, H., He, Y., Li, J., and Guo, J.: Effects of checkerboard barriers on the distribution of aeolian sandy soil particles and soil organic carbon, Geomorphology 338, 79-87, 2019.

Dong, Z., Fryrear, D., and Gao, S.: Modeling the roughness effect of blown-sand-controlling standing vegetation in wind tunnel, J. Desert Res. 20(3), 260-263, 2000.

Dupont, S., Bergametti, G., and Simoëns, S.: Modeling aeolian erosion in presence of vegetation, J. Geophys. Res. Earth Surf. 119(2), 168-187, 2014.

Dupont, S., Bergametti, G., Marticorena, B., and Simoëns, S.: Modeling saltation intermittency, J. Geophys. Res. Atmos. 118(13), 7109-7128, 2013.

Germano, M., Piomelli, U., Moin, P., and Cabot, W. H.: A dynamic subgrid-scale eddy viscosity model, Phys. Fluids A: Fluid Dyn. 3(7), 1760-1765, 1991.

Hatanaka, K. and Hotta, S.: Finite element analysis of air flow around permeable sand fences, Int. J. Numer. Methods Fluids 24(12), 1291-1306, 1997.

Huang, H. J., Bo, T. L., and Zhang, R.: Exploration of splash function and lateral velocity based on three-dimensional mixed-size grain/bed collision, Granul. Matter 19(4), 73, 2017.

Huang, H. J., Bo, T. L., and Zheng, X. J.: Numerical modeling of wind-blown sand on Mars, Eur. Phys. J. E 37(9), 80, 2014.

Huang, H. J.: Modeling the effect of saltation on surface layer turbulence, Earth Surf. Proc. Land. 45(15), 3943-3954, 2020.

Huang, N. and Wang, Z. S.: The formation of snow streamers in the turbulent atmosphere boundary layer, Aeolian Res. 23, 1-10, 2016.

Huang, N., Xia, X., and Tong, D.: Numerical simulation of wind sand movement in straw checkerboard barriers, Eur. Phys. J. E 36(9), 99, 2013.

Huang, N., Zhang, Y., and D'Adamo, R.: A model of the trajectories and midair collision probabilities of sand particles in a steady state saltation cloud, J. Geophys. Res. Atmos. 112(D8), 2007.

Inoue, M. and Pullin, D.: Large-eddy simulation of the zero-pressure-gradient turbulent boundary layer up to $Re_\theta = $ O (10^{12}), J. Fluid Mech. 686, 507-533, 2011.

Kok, J. F. and Renno, N. O.: A comprehensive numerical model of steady state saltation (COMSALT), J. Geophys. Res. Atmos. 114(D17), 2009.

Kok, J. F., Parteli, E. J., Michaels, T. I., and Karam, D. B.: The physics of wind-blown sand and dust, Rep. Prog. Phys. 75(10), 106901, 2012.

Li, B. and Sherman, D. J.: Aerodynamics and morphodynamics of sand fences: A review, Aeolian Res. 17, 33-48, 2015.

Li, B. W., Zhou, X. J., Huang, P. Z., Xu, X. W., Wang, Z. J., and Zhang, C. M.: Wind-Sand Damage and Its Control at Shaquanzi Section of Lan-xin Railway, Arid Zone Res. 15(4), 47-52, 1998.

Li, G., Wang, Z., and Huang, N.: A Snow Distribution Model Based on Snowfall and Snow Drifting Simulations in Mountain Area, J. Geophys. Res. Atmos. 123(14), 7193-7203, 2018.

Li, X., Xiao, H., He, M., and Zhang, J.: Sand barriers of straw checkerboards for habitat restoration in extremely arid desert regions, Ecol. Eng. 28(2), 149-157, 2006.

Lima, I. A., Araújo, A. D., Parteli, E. J., Andrade, J. S., and Herrmann, H. J.: Optimal array of sand fences, Sci. Rep. 7, 45148, 2017.

Lima, I. A., Parteli, E. J., Shao, Y. P., Andrade, J. S., Herrmann, H. J., and Araújo, A. D.: CFD simulation of the wind field over a terrain with sand fences: Critical spacing for the wind shear velocity, Aeolian Res. 43, 100574, 2020.

Liu, L. and Bo, T. L.: Effects of checkerboard sand barrier belt on sand transport and dune advance, Aeolian Res. 42, 100546, 2020.

Lund, T. S., Wu, X. H., and Squires, K. D.: Generation of turbulent inflow data for spatially-developing boundary layer simulations, J. Comput. Phys. 140(2), 233-258, 1998.

Ma, G. S. and Zheng, X. J.: The fluctuation property of blown sand particles and the wind-sand flow evolution studied by numerical method, Eur. Phys. J. E 34(5), 54, 2011.

McEwan, I. and Willetts, B.: Numerical model of the saltation cloud, Acta Mech. Supp. 1, 53-66, 1991.

Murphy, P. J. and Hooshiari, H.: Saltation in water dynamics, J. Hyd. Div. 108(11), 1251-1267, 1982.

Nepf, H. M.: Flow and transport in regions with aquatic vegetation, Annu. Rev. Fluid Mech. 44, 123-142, 2012.

Qiu, G. Y., Lee, I. B., Shimizu, H., Gao, Y., and Ding, G.: Principles of sand dune fixation with straw checkerboard technology and its effects on the environment, J. Arid. Environ. 56(3), 449-464, 2004.

Qu, J., Zu, R., Zhang, K., and Fang, H.: Field observations on the protective effect of semi-buried checkerboard sand barriers, Geomorphology 88(1-2), 193-200, 2007.

Rice, M. A., Willetts, B. B., and McEwan, I.: An experimental study of multiple grain-size ejecta produced by collisions of saltating grains with a flat bed, Sedimentology 42(4), 695-706, 1995.

Santiago, J., Martin, F., Cuerva, A., Bezdenejnykh, N., and Sanz-Andres, A.: Experimental and numerical study of wind flow behind windbreaks, Atmos. Environ. 41(30), 6406-6420, 2007.

Shao, Y. P. and Raupach, M.: The overshoot and equilibration of saltation, J. Geophys. Res. Atmos. 97(D18), 20559-20564, 1992.

Smagorinsky, J.: General circulation experiments with the primitive equations: I. The basic experiment, Mon. Weather Rev. 91(3), 99-164, 1963.

Vinkovic, I., Aguirre, C., Ayrault, M., and Simoëns, S.: Large-eddy simulation of the dispersion of solid particles in a turbulent boundary layer, Bound.-Layer Meteor. 121(2), 283, 2006.

Wang, T., Qu, J. J., and Niu, Q. H.: Comparative study of the shelter efficacy of straw checkerboard barriers and rocky checkerboard barriers in a wind tunnel, Aeolian Res. 43, 100575, 2020.

Wang, X., Chen, G., Han, Z., and Dong, Z.: The benefit of the prevention system along the desert highway in Tarim Basin, J. Desert Res. 19(2), 120-127, 1999.

Wang, X., Zhang, C., Hasi, E., and Dong, Z.: Has the Three Norths Forest Shelterbelt Program solved the desertification and dust storm problems in arid and semiarid China?, J. Arid. Environ. 74(1), 13-22, 2010.

Wang, X.: Discussion of sand hazard control along the Wu-Ji railway line, J. Desert Res. 16(2), 204-206, 1996.

Wang, Z. T. and Zheng, X. J.: A Simple Model for Calculating Measurements of Straw Checkerboard Barriers, J. Desert Res. 22(3), 229-232, 2002.

Werner, B.: A steady-state model of wind-blown sand transport, J. Geol. 98(1), 1-17, 1990.

Xu, B., Zhang, J., Huang, N., Gong, K., and Liu, Y.: Characteristics of turbulent aeolian sand movement over straw checkerboard barriers and formation mechanisms of their internal erosion form, J. Geophys. Res. Atmos. 123(13), 6907-6919, 2018.

Xu, J. L., Pei, Z. Q., and Wang, R. H.: Exploration of the width of the semi-buried straw checkerboard sand barriers belt, J. Desert Res. 2(3), 16-23, 1982.

Xu, X., Hu, Y., and Pan, B.: Analysis of the protective effect of various measures of combating drifting sand on the Tarim Desert Highway, Arid Zone Res. 15(1), 21-26, 1998.

Xue, M., Droegemeier, K. K., and Wong, V.: The Advanced Regional Prediction System (ARPS)-A multi-scale nonhydrostatic atmospheric simulation and prediction model. Part I: Model dynamics and verification, Meteorol. Atmos. Phys. 75(3-4), 161-193, 2000.

Xue, M., Droegemeier, K. K., Wong, V., Shapiro, A., Brewster, K., Carr, F., Weber, D., Liu, Y., and Wang, D.: The Advanced Regional Prediction System (ARPS)-A multi-scale nonhydrostatic atmospheric simulation and prediction tool. Part II: Model physics and applications, Meteorol. Atmos. Phys. 76(3-4), 143-165, 2001.

Xue, M., Droegemeier, K., Wong, V., Shapiro, A., and Brewster, K.: Advanced Regional Prediction System (ARPS) version 4.0 user's guide, Center for Analysis and Prediction of Storms, University of Oklahoma, 380, 1995.

Yang, A.: Closing sandy land to establish vegetation along a desert railway line, J. Desert Res.15(3), 308-311, 1995.

Zhang, C., Li, Q., Zhou, N., Zhang, J., Kang, L., Shen, Y., and Jia, W.: Field observations of wind profiles and sand fluxes above the windward slope of a sand dune before and after the establishment of semi-buried straw checkerboard barriers, Aeolian Res. 20, 59-70, 2016.

Zhang, K. C., Qu, J. J., Liao, K. T., Niu, Q. H., and Han, Q. J.: Damage by wind-blown sand and its control along Qinghai-Tibet Railway in China, Aeolian Res. 1(3-4), 143-146, 2010.

Zhang, S., Ding, G. D., Yu, M. H., Gao, G. L., Zhao, Y. Y., Wu, G. H., and Wang, L.: Effect of straw checkerboards on wind proofing, sand fixation, and ecological restoration in shifting Sandy Land, Int. J. Environ. Res. Public Health 15(10), 2184, 2018.

Zheng, X. J.: Mechanics of wind-blown sand movements, Springer Science & Business Media, 2009.

Zhou, Y. H., Li, W. Q., and Zheng, X. J.: Particle dynamics method simulations of stochastic collisions of sandy grain bed with mixed size in aeolian sand saltation, J. Geophys. Res. Atmos. 111(D15) , 2006.

Zou, X. Y., Cheng, H., Zhang, C. L., and Zhao, Y. Z.: Effects of the Magnus and Saffman forces on the saltation trajectories of sand grain, Geomorphology 90(1-2), 11-22, 2007.